3-1-2009

The Dust Cloud Around the White Dwarf G 29-38. II. Spectrum from 5 to 40 μm and Mid-Infrared Photometric Variability

William T. Reach
California Institute of Technology, reach@ipac.caltech.edu

Ted von Hippel
University of Texas at Austin, vonhippt@erau.edu

et al.

The Astrophysical Journal, 693:697–712, 2009 March 1 doi:10.1088/0004-637X/693/1/697

THE DUST CLOUD AROUND THE WHITE DWARF G 29-38. II. SPECTRUM FROM 5 TO 40 μm AND MID-INFRARED PHOTOMETRIC VARIABILITY

William T. Reach[1], Carey Lisse[2], Ted von Hippel[3,4,6], and Fergal Mullally[5]
[1] Infrared Processing and Analysis Center, MS 220-6, California Institute of Technology, Pasadena, CA 91125, USA; reach@ipac.caltech.edu
[2] Planetary Exploration Group, Space Department, Johns Hopkins University, Applied Physics Laboratory, Laurel, MD, USA
[3] Physics Department, Siena College, 515 Loudon Road, Loudonville, NY 12211, USA
[4] Department of Physics, Florida International University, 11200 SW 8th Street, Miami, FL 33199, USA
[5] Department of Astronomy, University of Texas, 1 University Station, C1400, Austin, TX 78712, USA
Received 2008 August 12; accepted 2008 August 21; published 2009 March 3

ABSTRACT

We model the mineralogy and distribution of dust around the white dwarf G29-39 using the infrared spectrum from 1 to 35 μm. The spectral model for G29-38 dust combines a wide range of materials based on spectral studies of comets and debris disks. In order of their contribution to the mid-infrared emission, the most abundant minerals around G29-38 are amorphous carbon ($\lambda < 8$ μm), amorphous and crystalline silicates (5–40 μm), water ice (10–15 and 23–35 μm), and metal sulfides (18–28 μm). The amorphous C can be equivalently replaced by other materials (like metallic Fe) with featureless infrared spectra. The best-fitting crystalline silicate is Fe-rich pyroxene. In order to absorb enough starlight to power the observed emission, the disk must either be much thinner than the stellar radius (so that it can be heated from above and below) or it must have an opening angle wider than 2°. A "moderately optically thick" torus model fits well if the dust extends inward to 50 times the white dwarf radius, all grains hotter than 1100 K are vaporized, the optical depth from the star through the disk is $\tau_{\|} = 5$, and the radial density profile $\propto r^{-2.7}$; the total mass of this model disk is 2×10^{19} g. A physically thin (less than the white dwarf radius) and optically thick disk can contribute to the near-infrared continuum only; such a disk cannot explain the longer-wavelength continuum or strong emission features. The combination of a physically thin, optically thick inner disk and an outer, physically thick and moderately optically thin cloud or disk produces a reasonably good fit to the spectrum and requires only silicates in the outer cloud. We discuss the mineralogical results in comparison to planetary materials. The silicate composition contains minerals found from cometary spectra and meteorites, but Fe-rich pyroxene is more abundant than enstatite (Mg-rich pyroxene) or forsterite (Mg-rich olivine) in G29-38 dust, in contrast to what is found in most comet or meteorite mineralogies. Enstatite meteorites may be the most similar solar system materials to G29-38 dust. Finally, we suggest the surviving core of a "hot Jupiter" as an alternative (neither cometary nor asteroidal) origin for the debris, though further theoretical work is needed to determine if this hypothesis is viable.

Key words: infrared: stars – stars: individual (G29-38, WD 2326+049) – white dwarfs

Online-only material: color figures

1. INTRODUCTION

The end state of stellar evolution for most types of star is a white dwarf. Planetary material is common around main-sequence stars (Backman & Paresce 1993; Rhee et al. 2007; Trilling et al. 2008). Part of the planetary system is expected to survive the violent, late stages of stellar evolution (Debes & Sigurdsson 2002). Thus, it is to be expected that planetary materials are present around white dwarfs. But since white dwarfs are so underluminous, this material is normally impossible to detect via reflected light or thermal emission if it is distributed like the solar system (with its inner portion destroyed out to at least the maximum radius of the red giant/asymptotic giant branch (AGB) photosphere). Young, hot white dwarfs, where debris can be detected even at 100 AU from the star (Su et al. 2007), are the exception to this rule. Planetary material can become detectable if it moves sufficiently close to a star, for example via gravitational perturbations such as produce comets in the inner solar system (from their Kuiper Belt or Oort Cloud homes) and meteorites on the surface of Earth (from their asteroid belt homes). Jura (2003) explained how an asteroid can pass sufficiently close to a white dwarf to be tidally disrupted, leaving a disk of dust near the star. Sun-grazing comets in the solar system pass within similar distances. The new and growing class of dusty, metal-rich white dwarfs (classified as DAZd, where D = white dwarf, A = mostly hydrogen atmosphere, Z = trace atmospheric metals, d = dusty) allow a unique window into planetary systems (von Hippel et al. 2007).

The first-known DAZd star, and the one with the brightest infrared excess, is Giclas 29-38 (WD 2326+049; G29-38 hereafter). Its effective temperature has been estimated in the range 11,800–12,100 K with surface gravity $\log g$ in the range 8.14–7.90 (e.g., Bergeron et al. 2004; Koester et al. 2005). In Holberg & Bergeron (2006), the model corresponding to the lowest estimated T and highest g has radius 8100 km and mass 0.69 $M_{\odot}$, while the model corresponding to the highest T and lowest g has radius 9650 km and mass 0.55 $M_{\odot}$. At wavelengths longer than 2.5 μm the spectrum is completely dominated by non-photospheric thermal emission with color temperatures 300–900 K. In Paper I (Reach et al. 2005a), we measured the spectrum of this star from 5.5 to 14 μm, revealing a remarkably strong emission feature from 9 to 11 μm that is typical of small (less than 2 μm radius) silicate grains. The brightness of the disk permits spectroscopy at sufficient signal-to-noise ratio (S/N) to study the dust mineralogy. We have now measured the

[6] Visiting Research Scientist at Florida International University.

Table 1
Spitzer Observing log for G29-38

Date	AORID	Instrument	Wavelengths
2004 Nov 26	10119424	IRAC	4.5, 8 μm
2005 Nov 26	11124224	IRAC	3.6, 4.5, 5.8, 8 μm
2004 Dec 2	10149376	MIPS	24 μm
2004 Dec 8	10184192	IRS	5.2–14.2 μm
2005 Dec 23	13835264	IRAC	3.6, 4.5, 5.8, 8 μm
2006 Jun 30	13828096	IRS	5.2–36 μm

Table 2
Mid-infrared Fluxes of G29-39 (mJy)[a]

	2004 Nov 26 10:54	2004 Nov 26 10:58	2005 Dec 23 23:23
3.6 μm		8.37 ± 0.01	8.10 ± 0.03
4.5 μm	8.88 ± 0.02	8.87 ± 0.01	
5.8 μm		8.37 ± 0.02	8.28 ± 0.07
8.0 μm	8.73 ± 0.03	8.72 ± 0.02	

Note. [a] Uncertainties are statistical uncertainty in the weighted mean of the flux measurements from all frames taken during each observing sequence.

infrared spectrum out to 35 μm, and in this paper we discuss dust cloud models and compositions in more detail.

After presenting the new observations, analyzing the variability, and compiling the spectral energy distribution in Section 2, we model the disk in several different ways. In Section 3, we use a wide mix of minerals and a simple temperature distribution to determine likely constituents of the disk based on spectral features. In Section 4, we present optically thin shell, moderately optically thick disk, and optically thick thin disk models. In Section 5, we present constraints based on variability. In Section 6, we tie together the evidence gleaned from comparing the models to the observations.

2. OBSERVATIONS

Table 1 shows a log of observations with the *Spitzer Space Telescope* (Werner et al. 2004). The Infrared Spectrograph (IRS; Houck et al. 2004) observations were performed in "staring" mode, wherein the source was placed on each of two nod positions on each of the slits and orders. IRS data were processed with the S16 pipeline (with backgrounds subtracted by differencing nods) and extracted using optimal extraction in the *Spitzer* Science Center's data analysis tool SPICE. The 4.5, 8, and 24 μm observations described in Paper I were supplemented by archival Infrared Array Camera (IRAC; Fazio et al. 2004) 3.6, 4.5, 5.8, and 8 μm observations. Annular aperture photometry was performed on each IRAC basic calibrated image with a 4 pixel on-source radius and 8–20 pixel background annulus; array-location-dependent, aperture-loss, and pixel-phase photometric corrections were applied; and the uncertainty of each image's photometry was determined by combining uncertainties due to photon statistics and background removal (see Reach et al. 2005b).

2.1. Variability of the Mid-infrared Flux

The variability of the mid-infrared flux of G29-38 can be constrained with the IRAC photometry.[7] Fluxes are shown in Table 2. The brightness of the star on each basic calibrated image from each observing sequence was measured, corrected for the array-location-dependent response, then a weighted mean and statistical uncertainty in weighted mean computed. The absolute calibration uncertainties are not included because we are comparing fluxes from the same instrument; IRAC photometry has been shown to be stable to better than 1% (Reach et al. 2005b). To obtain the highest S/N from each image for repeatability, we found that an aperture radius of 4 pixel was optimal. The S/N was 230, 2008, 90, and 130 at 3.6, 4.5, 5.8, and 8 μm, respectively. At 4.5 and 8 μm, the star was observed in two independent observations just a few minutes apart, yielding identical mean fluxes; the flux differences are $-0.1\% \pm 0.2\%$ and $-0.1\% \pm 0.3\%$, respectively. At 3.6 and 5.8 μm, the star was observed with different Astronomical Observing Requests (AORs) separated by 13 months. The star was fainter in the second epoch by $-3.3\% \pm 0.4\%$ at 3.6 μm (and a statistically insignificant $-1.0\% \pm 0.8\%$ at 5.8 μm). The brightness difference at 3.6 μm is likely due to short-term fluctuations in the star, to which we turn now.

The variability of the mid-infrared flux over shorter timescales can be assessed from the individual images taken in 2004 November. By the design of IRAC (Fazio et al. 2004), the 3.6 and 5.8 μm channels observe simultaneously, as do the 4.5 and 8 μm channels. The sequence of events was as follows, with times given relative to the first image at 2004 November 26 10:54:11.8 UT:

00:00 the star is placed in the 4.5 + 8 μm field of view and a short (1.2 s) frame is taken;

00:03 five consecutive dithers, consisting of a 30 s frame and a short telescope slew, are performed;

04:34 the telescope is moved to re-center the star in the 4.5 + 8 μm field of view and a short (1.2 s) frame is taken;

04:37 19 consecutive dithers, consisting of a 30 s frame and a short telescope slew, are performed;

18:22 the telescope is moved to center the star in the 3.6 + 5.8 μm field of view;

18:22 19 consecutive dithers, consisting of a 30 s frame and a short telescope slew, are performed; then

30:51 the sequence is complete.

Figure 1 shows the flux versus time. The scatter in the photometric measurements is significantly larger than their uncertainties, especially at 3.6 μm. To assess the harmonic content of the time series, we computed the periodogram as described by Scargle (1982). Figure 2 shows the periodograms at the four IRAC wavelengths. The time series cannot be described by a simple period, but instead contain variation on a range of timescales. This is characteristic of ZZ Ceti variable stars (Kleinman et al. 1998). The peak in the 3.6 μm amplitude at 190 s is highly significant (14σ), as is the harmonic content at 300–440 s. None of the other harmonic contents is significant, at the sampling frequency and S/N level of these observations, except some power (3.3σ) at $\sim$ 220 s at 4.5 μm.

The flux variations seen with IRAC are similar to those seen at Palomar by Graham et al. (1990), who observed them simultaneously at wavelengths dominated by the photosphere (B, J) and the infrared excess (K band). They found fluctuations at periods 181 and 243 s in the K band, with no corresponding ones at the J band. Our IRAC 3.6 μm results confirm the significant fluctuations at $\sim$ 190 s. The amplitude of the fluctuations is $\sim$ 4% at 3.6 μm, while Graham et al. (1990) found 2.5% variations

[7] We tested the IRS observations for variability, but there was no clear evidence. The IRS observing strategy provided six samples along 60 s ramps in each subslit. The flux varied by less than 4% among the shortest wavelength spectra, with no wavelength dependence detectable above the noise.

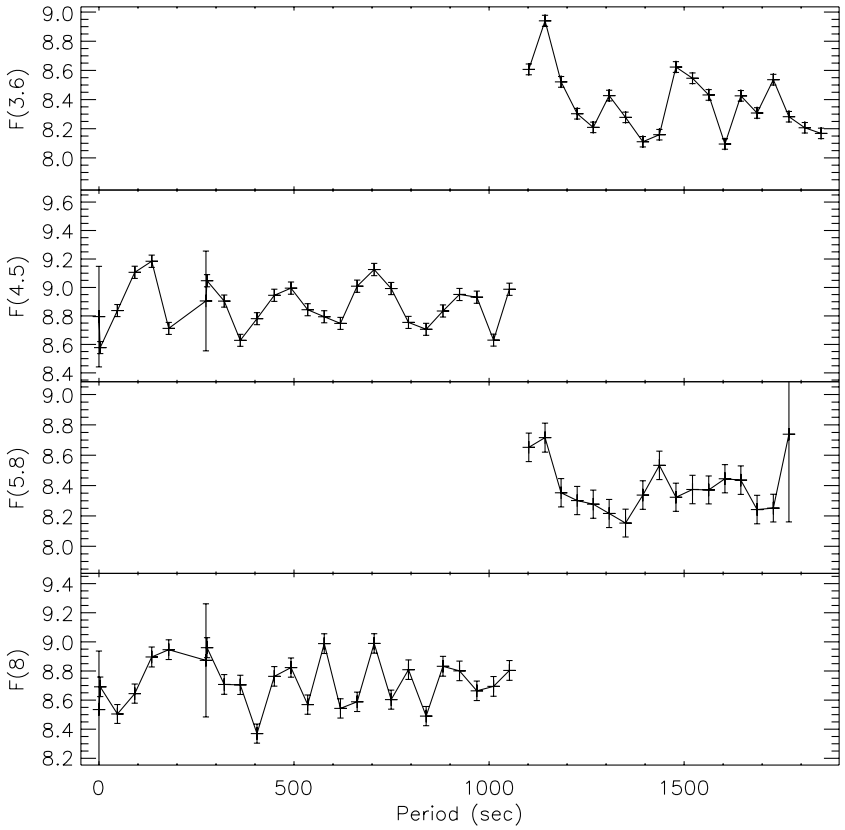

Figure 1. Flux vs. time for each of the IRAC channels (from top to bottom: 3.6, 4.5, 5.8, and 8 μm wavelength). The time begins with the first frame of the entire sequence (which combines two AORs) at 2004 November 26 10:54:11.28 UT. Each point is a flux measurement from a single image, with the statistical uncertainty of the aperture photometry performed as described by the IRAC calibration procedure (Reach et al. 2005b). Line segments simply connect the data points. The high error points at 4.5 and 8 μm are the short frames taken just at the beginning of each of the two AORs. All four plots are scaled to show the same dynamic range (from -6% to +8.4%, centered on the median).

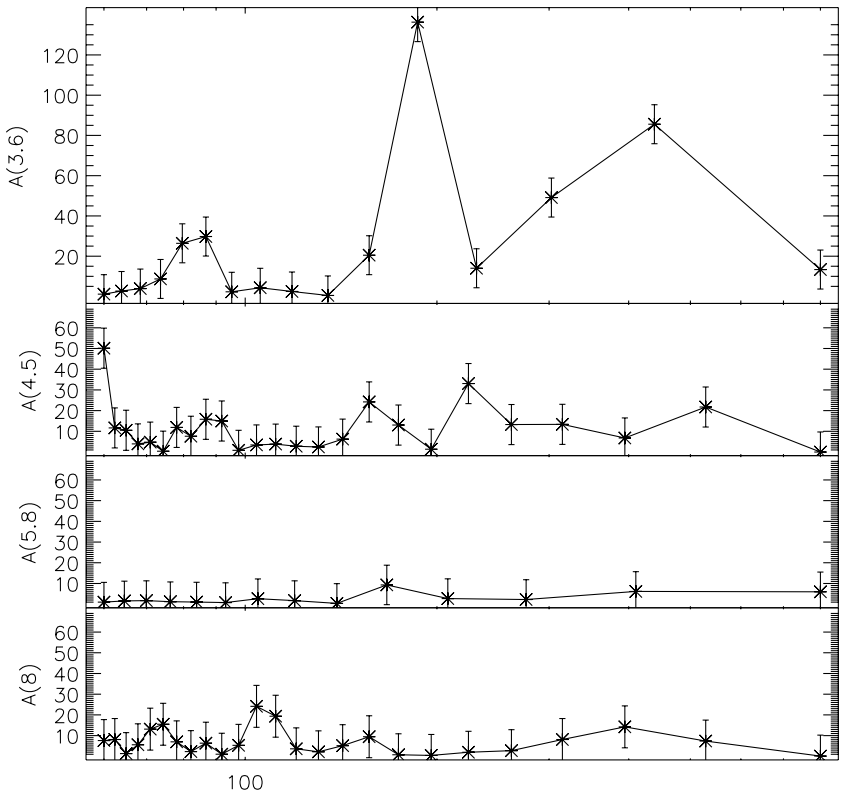

Figure 2. Scargle periodograms of the time series from the IRAC 2004 November 26 observations. Each panel has the same scale both horizontally and vertically; the 3.6 μm panel is twice as large because the amplitudes are much higher. The periods ($2\pi/\omega$, where ω is the angular frequency) are displayed on a logarithmic stretch.

at 2.2 μm. The stellar photosphere must be subtracted before interpreting these results. At 2.2 (3.6) μm, the photosphere contributes 66% (18%) of the total flux. If we assume the infrared photosphere is constant, and the fluctuations are due to the disk, then the amplitude of disk fluctuations at 2.2 (3.6) μm is 7% (5%), i.e., very similar, with *K* band possibly slightly higher in amplitude. Fluctuations at 4.5, 5.8, and 8 μm are not detected in the periodogram, with upper limit $\sim$ 5%, 5%, and 3% of the total flux, or 5%, 5%, and 3% of the infrared excess above photosphere (2σ limits). The upper limit at 8 μm, and the trend such that fluctuations are most significant at 2.2 and 3.6 μm with a rapid decrease in amplitude at longer wavelengths, are significant and indicate that the fluctuations are due to an emitting region with a relatively high (greater than 1000 K) color temperature.

2.2. Compilation of the Spectral Energy Distribution

In order to model the mineralogy and dust distribution around G29-38, we need to combine the observed data from the near-infrared through mid-infrared, correcting for calibration errors as well as source variability. This is in fact not possible, since the temporal sampling of the photometry is inadequate, and the observations are not contemporaneous. We therefore must assemble the various portions of the spectrum in such a way as to make them most plausibly "connected." In principle, there is a scale factor for each wavelength range that depends on the epoch. The amplitude of the scale factor, due to source variability, may reach up to $\sim$ 10% in the near-infrared and should be less than 5% at longer wavelengths. Calibration uncertainties range from $\sim$ 3% in the optical to 5% for IRAC and MIPS to 10% for IRS. The range of plausible scale factors is then 5%–10% across all wavelengths.

We first ensured that the spectroscopy and photometry were in accord. The IRAC fluxes must be corrected for the spectral shape of the source first. For the IRAC 8 μm channel, which is fully covered by the IRS spectrum, we integrated the IRS spectrum appropriately (Reach et al. 2005b) over the passband to calculate the color correction $K = 1.16$ (where the corrected flux is the "observed" flux from the IRAC calibration divided by *K*) and applied this correction to the photometry. The IRAC 8 μm flux density can then be compared directly to the IRS spectrum: the flux at the nominal wavelength 7.872 μm is 7.19 mJy from IRAC and 7.30 mJy from IRS, a deviation of only 1.5%, well within the calibration error budget. The IRAC 3.6, 4.5, and 5.8 μm flux density required only very small color corrections: the spectrum has a color temperature $\sim$ 1100 K at these wavelengths, for which the corrections are 0.995, 0.996, and 0.996, respectively. The absolute fluxes from IRAC and IRS at 5.831 μm are 7.76 and 7.54 mJy, showing that the instrument cross-calibration is good. The observed MIPS 24 μm flux was divided by a color correction of 0.97 to account for the wide spectral response of the filter and detector. For IRAC and IRS, we therefore find that there is no need for a relative rescaling; that is, the measured flux densities averaged over their exposure times at their epoch of observation agree well, whether due to averaging of *or* lack of variability.

To remove the white dwarf photosphere from the spectra, we use a model atmosphere for $T = 12{,}000$ K and $\log g = 8$ covering 0.35–60 μm (courtesy D. Koester 2005, private communication), normalized using Two Micron All Sky Survey (2MASS) photometry ($J = 13.132 \pm 0.029$, $H = 13.075 \pm 0.022$, $K_s = 12.689 \pm 0.029$) and optical spectrophotometry from Palomar (Greenstein & Liebert 1990). In fact, the optical and 2MASS photometry cannot both agree with the model spectrum. If we normalize the white dwarf model at the 2MASS *J* band, then the model would underpredict the visible flux by 8%. The near-infrared spectrum obtained by Kilic et al. (2006) with the Infrared Telescope Facility (IRTF) also disagrees with the 2MASS photometry; if we normalize the white dwarf model by the 2MASS *J*-band flux, then we underpredict the IRTF spectrum by 18%. The low flux observed by 2MASS is likely due to the variability of the white dwarf. The shape of the IRTF spectrum follows the model closely at wavelengths shorter than 1.6 μm; the infrared excess is evident at wavelengths beyond 1.7 μm. To obtain a joined spectral energy distribution we proceed as follows: (1) normalize the white dwarf model to match the optical photometry; (2) scale the 2MASS photometry by a factor of 1.087 to match the model at *J* band; (3) rescale the IRTF spectrum by 0.92 to match the white dwarf model at 0.8–1.3 μm; and (4) rescale the 2MASS photometry and IRTF spectra by a factor of 1.2 so that the red end of the IRTF spectrum (2.4 μm) is plausibly consistent with the IRAC 3.6 μm photometry. Plausible consistency here was defined as allowing a blackbody to pass through the IRAC 3.6 μm and 2MASS K_s photometry for color temperatures 800–1200 K to within the error bars, and keeping the IRTF and 2MASS photometry consistent at 2.17 μm. The uncertainties were taken to be a root-sum-square combination of the measurement uncertainties and 10% of the brightness of the photosphere, to account for scaling uncertainties in the photospheric subtraction.

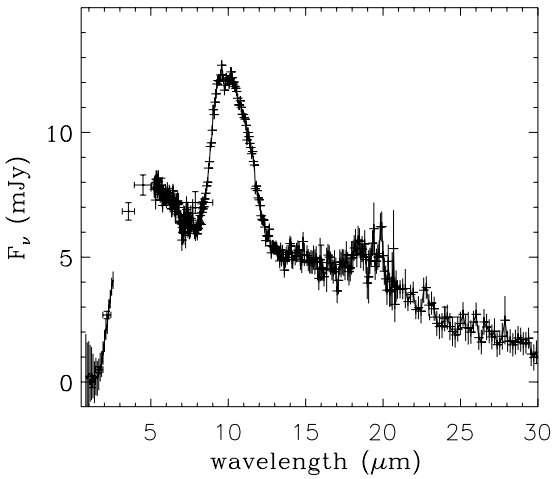

Figure 3. Combined spectra and photometry (using 2MASS, IRTF, IRAC, MIPS, and IRS) of G29-38 with stellar photosphere removed.

Figure 3 shows the combined spectrum of the infrared emission after subtracting the stellar photospheric emission. The combined scalings yield near-infrared photometry and spectrum effectively at the same epoch (in terms of variability) as the mid-infrared photometry.

3. MINERALOGY

The composition of the dust around G29-38 was determined by comparing the spectra to those of a set of constituent materials, using a fitting method that has been used for comet Hale–Bopp, the Deep Impact ejecta from comet 9P/Tempel 1, and the dust around the stars HD 100546, HD 69380, and HD 113766 (Lisse et al. 2006, 2007a, 2007b, 2008). Details of this model are given in Lisse et al. (2008). In this section, we model the emitting region as an optically thin dust torus. We apply this simple model to G29-38 to allow direct comparison

to dust in other astronomical systems, but we will revisit the mineralogy below when testing more sophisticated models.

3.1. Particle Sizes and Temperatures

A toroidal model is motivated by the single temperature distributions found for many of the stars studied by Beichman et al. (2006) and Chen et al. (2006) as well as the narrow dust structures found in many of the *Hubble Space Telescope* images of debris disks (Kalas et al. 2005, 2006). The best-fit temperature of the smallest dust particles (0.1–1 μm), which superheat substantially above Local Thermal Equilibrium (LTE), is $T_{\max} =$ 890 K for the olivines, 850–890 K for the pyroxenes, and 930 K for the amorphous carbon. The largest particles in our calculation, with radius 1000 μm, are set to $T_{\rm LTE} = 600$ K, and dust of intermediate size is scaled between the two extremes (Lisse et al. 2006). Using the Tempel 1 ejecta temperatures as a guide (where we found olivines at 340 K and amorphous carbon at 390 K at 1.51 AU from the Sun, where $T_{\rm LTE} =$ 230 K), and allowing for an G29-38 stellar luminosity that is 2×10^{-3} $L_\odot$, we estimate a location for the hot dust $\sim$ 150 stellar radii from the white dwarf. The location of colder dust, capable of supporting a stable water ice component at 200 K, is at $> 10^3$ stellar radii ($> 8 \times 10^{11}$ cm). While differing by at least a factor of 9, this range of distances is still small, suggesting material in tight orbit around the WD. The best-fit single continuum temperature to the 7–35 μm *Spitzer* spectrum is 950 K, close to the amorphous carbon temperature. As seen in the Tempel 1 ejecta from the Deep Impact experiment (Lisse et al. 2006), the amorphous carbon dominates the continuum behavior as it has a featureless emissivity and is the hottest material, thus contributing most to the short-wavelength emission.

The best-fit size distribution $dn/da \propto a^{-3.7\pm0.2}$ argues for dust surface area dominated by small particles, but dust mass dominated by large particles. A system in collisional equilibrium would demonstrate a PSD $\propto a^{-3.5}$ (Dohnanyi 1969; Durda & Dermott 1997); for "real" systems a size distribution even steeper than $a^{-3.5}$ at small sizes is expected in a collisional cascade because of the dependence of particle strength on size (O'Brien & Greenberg 2003).

The total dust mass required to explain the *Spitzer* IRS spectrum (i.e., mass in particles of 0.1–10 μm in size that contribute appreciably to the χ^2_ν value of the fit to the infrared spectrum) is $\sim 2 \times 10^{19}$ g. Extrapolating (using the best-fit size distribution) from a maximum size of 10 μm to 1 cm would increase the mass by a factor of 8. A total cloud mass of order 10^{19} g compressed into a solid sphere of average density 2.5 g cm^{-3} (i.e., rocky silicate material) would have a radius of 10 km, equivalent to a single, small asteroid or large comet. The surface area of *detected* particles is 5×10^{22} cm^2. If this dust is in an annulus of inner radius 7×10^{10} cm ($90R_*$) extending to twice that radius, then the areal filling factor of grains viewed from above the disk is of order unity. The optically thin model is thus unlikely to apply, although most of the observed emission (in particular the spectral features) must arise from the optically thin parts of the disk. We address the optical depth effects in the modeling sections, but we proceed first (with caution) to discuss the mineralogy from the optically thin fits.

3.2. Dust Composition

Over 80 different species were tested for their presence in the spectra. The material spectra were selected by their reported presence in meteorites, in situ comet measurements, YSOs, and debris disks (Lisse et al. 2006). Consultations with members of the *Stardust* team and examination of the interplanetary dust particle (see review by Bradley 2002) and the astromineralogical literature (see review by Molster & Waters 2003) pointed to the most likely mineralogical candidates to be found in the dust. Materials with emissions matching the strong features in the *Spitzer* emissivity spectra were also tested. The list of materials tested against the *Spitzer* spectra included multiple silicates in the olivine and pyroxene class (forsterite, fayalite, clino- and orth-enstatite, augite, anorthite, bronzite, diopside, and ferrosilite); phyllosilicates (saponite, serpentine, smectite, montmorillonite, and chlorite); sulfates (gypsum, ferrosulfate, and magnesium sulfate); oxides (various aluminas, spinels, hibonite, magnetite, and hematite); Mg/Fe sulfides (pyrrohtite, troilite, pyrite, and niningerite); carbonate minerals (calcite, aragonite, dolomite, magnesite, and siderite); water ice, clean and with carbon dioxide, carbon monoxide, methane, and ammonia clathrates; carbon dioxide ice; graphitic and amorphous carbon; and polycyclic aromatic hydrocarbons (PAH). Of these materials, a small, unique subset was found necessary to properly fit the *Spitzer* data. Sources for the data included: for *silicates*, the Jena Database of Optical Constants for Cosmic Dust[8] (Dorschner et al. 1995; Jäger et al. 1998, 2003), the Mars Global Surveyor Thermal Emission Spectrometer database[9], and W. Glaccum (2007, private communication), as well as emission spectra from Koike et al. (2003) and Chihara et al. (2002); for *carbonates*, Kemper et al. (2002); for *sulfides*, Keller et al. (2002) and Kimura et al. (2005); for *amorphous carbon*, Edoh (1983); for *PAH*, Li & Draine (2001).

We determined the reduced χ^2 for the model fit to the data for thousands of combinations of minerals. All models with reduced χ^2 values large than the 95% confidence limit were excluded from consideration. The range of constituent abundances was determined by varying the amount of a material and finding where the model exceeded the 95% confidence limit. Only constituents with abundances significantly above zero were included in the final best fit. Table 3 shows the composition of the best-fit model. For each entry, we also show the reduced χ^2 for the model if that constituent is deleted. Upper limits for nondetected species are included in Table 3 based on the 95% confidence level amplitude of the constituent when it is included in the fit.

Figure 4 shows the best-fit spectral model for G29-38. In order of their contribution to the mid-infrared emission, the contributing minerals are amorphous carbon; amorphous olivine; crystalline silicates ferrosilite ($FeSiO_3$), fayalite (Fe_2SiO_4), diopside ($MgCaSi_2O_6$), and enstatite ($MgSiO_3$); metal sulfides ($Mg_{10}Fe_{90}S$); and water ice. Figure 5 shows the spectral model after removal of the best-fitting amorphous silicates that dominate the overall spectral shape. The fit to the IRS data (5.2–35 μm) is excellent, with $\chi^2_\nu = 1.03$.

The composition of the dust surrounding G29-38, as determined by modeling of the *Spitzer* IRS spectrum, is unusual when compared to circumstellar dust in other environments. Amorphous olivine is present, as in the other systems that have been modeled with the same technique. But the relative lack of crystalline olivine, and the strong prevalence of Fe-rich silicates, make the G29-38 material distinct from other systems. The mix of crystalline pyroxenes and amorphous olivines may be indicative of "aged" dusty material. No PAHs, carbonates, or

[8] http://www.astro.uni-jena.de/Laboratory/OCDB.
[9] http://tes.asu.edu.

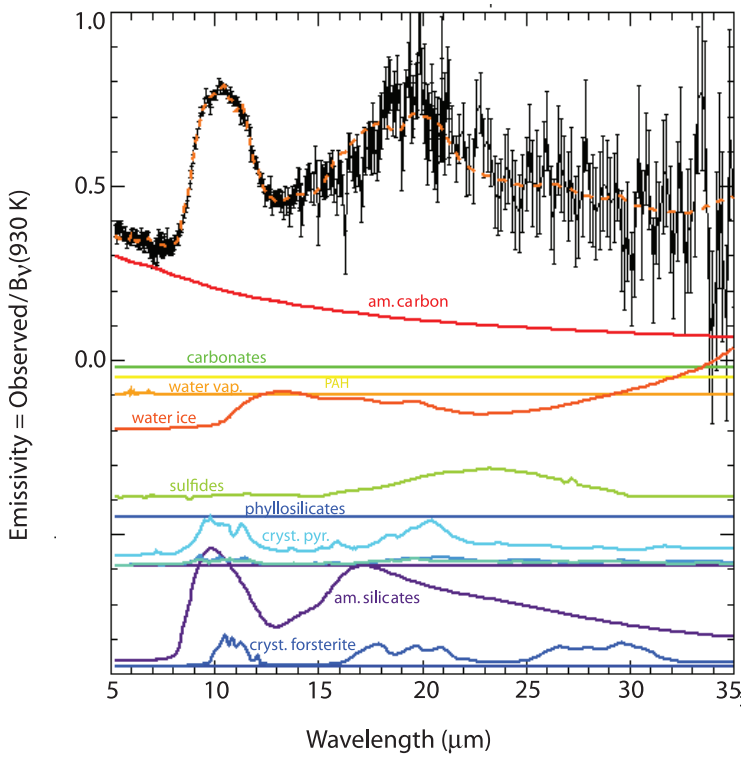

Figure 4. Emissivity spectrum of the dust around G29-38. The observed spectrum has been divided by a 930 K blackbody and fitted with a linear combination of 12 minerals. The shape of each mineral's emissivity, normalized by its fitted amplitude to the G29-38 emissivity, is shown separately by a colored line (offset vertically for clarity): red = amorphous carbon, bright green = carbonates (zero amplitude), yellow = PAH (zero amplitude), light orange = water vapor (zero amplitude), deep orange = water ice, olive green = sulfides, represented here by niningerite, blue = phyllosilicates (zero amplitude), light blue = crystalline pyroxenes (ferrosilite, diopside, and orthoenstatite, in order of 20 μm amplitude), purple = amorphous olivine, and dark blue = crystalline olivines (forsterite and fayalite, in order of 20 μm amplitude).

(A color version of this figure is available in the online journal.)

Table 3
Composition of the Best-Fit Model[a] to the *Spitzer*/IRS G29-38 Spectrum

Species	Weighted[b] Surface Area	Density (g cm^{-3})	Mol. Wt. (Relative)	$N_{\rm moles}$[c]	$T^{\rm d}_{\rm max}$ (K)	χ^2 if Excluded
Detections						
Amorph Olivine ($MgFeSiO_4$)	0.33	3.6	172	0.69	890	90.6
Fayalite (Fe_2SiO_4)	0.08	4.3	204	0.17	890	2.91
FerroSilite ($Fe_2Si_2O_6$)	0.11	4.0	264	0.17	890	9.85
Diopside ($CaMgSi_2O_6$)	0.05	3.3	216	0.076	890	2.05
OrthoEnstatite ($Mg_2Si_2O_6$)	0.04	3.2	200	0.064	890	1.98
Niningerite ($Mg_{10}Fe_{90}S$)[e]	0.10	4.5	84	0.53	890	1.49
Amorph Carbon (C)	0.28	2.5	12	5.83	930	>100
Water Ice (H_2O)	0.29	1.0	18	1.61	220	5.82
Upper Limits and Nondetections						
Forsterite[Koike](Mg_2SiO_4)	0.02	3.2	140	0.046	890	1.15
Amorph Pyroxene ($MgFeSi_2O_6$)	0.00	3.5	232	0.09	890	1.04
Smectite/Notronite[f]	0.00	2.3	496	0.03	890	1.04
Water Gas (H_2O)	0.01	1.0	18	$\leqslant$0.00	220	1.04
Magnesite ($MgCO_3$)	0.00	3.1	84	$\leqslant$0.00	890	1.04
Siderite ($FeCO_3$)	0.00	3.9	116	$\leqslant$0.00	890	1.04
PAH ($C_{10}H_{14}$)	0.00	1.0	(178)	$\leqslant$0.011	N/A	1.04

Notes.
[a] Best-fit model $\chi^2_\nu = 1.04$ with power-law particle size distribution $dn/da \propto a^{-3.7}$, 5–35 μm range of fit, 336 degrees of freedom (dof).
[b] Weight of the emissivity spectrum of each dust species required to match the G29-38 emissivity spectrum.
[c] $N_{\rm moles}(i)$ is the Density/Molecular Weight × Normalized Surface Area for mineral i. Errors are ±15% (1σ).
[d] All temperatures are ±20 K (1σ).
[e] We use the name niningerite to refer to $Mg_xFe_{1-x}S$. A niningerite composition of $Mg_{25}Fe_{75}S$ may fit the data better.
[f] $Na_{0.33}Fe_2(Si,Al)_4O_{10}(OH)_2 \cdot 3H_2O$.

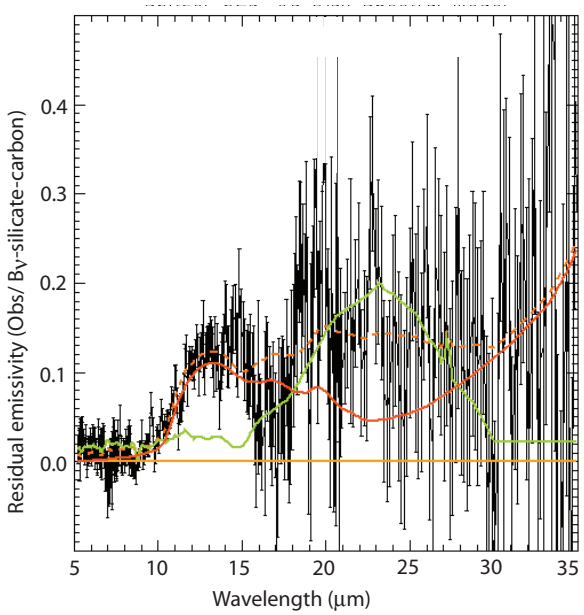

Figure 5. Emissivity spectrum as in Figure 4, but after the removal of the best-fitting silicates and carbon. The residuals are well fitted by a combination of water ice (deep orange, dashed and solid are two temperatures) and metal sulfides (olive green). The water ice is at temperature 200 K, and cannot be in the same location as the 930 K dust. Whereas the dust is $\sim 10^{11}$ cm from the star, the water ice must be further, $\sim 10^{13}$ cm, at the outer edge of an extended disk.

(A color version of this figure is available in the online journal.)

water gas are seen, reflecting a total lack of primitive nebular material. Some metal sulfides appear to be present, suggesting temperatures as low as $\sim$ 600 K in the observed dust; 600–700 K is the temperature range for vaporization/condensation of ferrosulfides. Given that the best-fit continuum temperature for the spectrum is 930 K (dominated by the short-wavelength emission from 0.1 to 1.0 μm amorphous carbon particles), either the carbon is superheated beyond the temperature of the metal sulfides, which may be present in larger, cooler particles, or there is a distribution of dust locations and effective temperatures, i.e., a disk-like structure.

3.3. Water Ice

The detection of water ice emission in the spectrum is curious. In a vacuum, water ice sublimates at temperatures above $\sim$ 200 K. Thus, water ice cannot be in direct physical contact with the rest of the hot dust detected in the infrared spectrum. Either the dust must be continuously created, or it must reside in a physical location removed from the rest of the dust reservoir. Since no water vapor is detected at 6 μm, where there are strong features that should be detected if water were present in significant quantities (Lisse et al. 2006; Woodward et al. 2007), no appreciable ongoing sublimation can be occurring. Water vapor is ionized within $\sim 10^3$ s, if we scale from the lifetime of water at 1 AU from the Sun ($\sim 10^6$ s; Schleicher & A'Hearn 1988) according to the luminosity of G29-38 ($2 \times 10^{-3}\ L_\odot$). There would still be a steady-state amount of water vapor present if the ice is sublimating. Thus, it appears that the water ice is at a large remove from the rest of the warm circumstellar dust, and the water ice is found in the IRS beam (i.e., within 5×10^{14} cm ($7 \times 10^5 R_*$) of the star).

In Paper I, we showed that a range of temperatures is required to match the photometry out to 24 μm, with a two-temperature fit having 890 and 290 K color temperatures. Thus, we already suspected either a continuous range of dust temperatures or the presence of two dust reservoirs, one hot and one cold. For G29-38, the ice (or ice-coated grains) must be located at greater than 10^{12} cm ($2000 R_*$) from the star, which, while farther than the dust that dominates the mid-infrared spectrum, is still very close to the star. Cold, icy dust around other stars, at locations comparable to the solar system's Kuiper Belt, is common, being present around 15%–20% of all stars (Bryden et al. 2006). The ice detected around G29-38 is closer to the star than the far-infrared debris disks at $\sim$100 AU (10^{15} cm) radius commonly seen around main-sequence stars (Bryden et al. 2006), and the present location of the icy grains would have been within the star when G29-38 was in its red giant or AGB stage. The source of this cold, presumably icy, material is likely to be the same parent bodies that create the dust closer to the star. We will return to the possible parent body natures in the Discussion section, but we should point out now that the presence of H_2O is well established in asteroids (especially outer belt), meteorites (as water of hydration as well as signatures of aqueously altered mineralogy), comets, and planets. The H_2O in any of these bodies would freeze if it were liberated by disintegration of these bodies and survive out to greater than 10^{12} cm from the white dwarf, owing to its small luminosity.

4. DISTRIBUTION OF MATERIAL AROUND THE STAR

Two possible disk models are considered; these are illustrated in Figure 6 and discussed in turn in the following sections. The models will be fitted to a combination of *Spitzer* spectroscopy and photometry, 2MASS photometry, and the near-infrared spectrum, after the removal of the photosphere model and scaling to a common epoch (Section 2.2).

4.1. Physically Thick Disk

If the optical depth through the dust cloud around G29-38 is optically thin at the wavelengths of the observed emission, then the spectrum is determined by simply integrating the density distribution, weighted by the Planck function at the local temperature, through the cloud. If the cloud is optically thin at visible wavelengths, where the spectrum of the white dwarf peaks, then the dust heating is simply determined by the integrated absorption of the star's distance-diluted spectrum by each grain. We can place some constraints on whether such a model can apply. First, the cloud can only emit as much energy as it absorbs from the star. Let us consider a flattened torus, defined in spherical coordinates r, θ (with r the distance from the star and θ the angular separation from the equatorial plane) as having nonzero density for $R_1 < r < R_2$ and $\theta < \theta_{\frac{1}{2}}$. Since the dust luminosity is $f = 3\%$ of the star luminosity, the opening half-angle of the torus must be at least $\theta_{\frac{1}{2}} > f/2$ radians, i.e., $\theta_{\frac{1}{2}} > 0.^\circ 8$. A thinner torus simply cannot intercept enough starlight to emit the observed luminosity. The constraint does not apply to a disk thinner than the radius of the star, nor to a warped disk, as discussed in the following sections.

Of critical importance to the radiative transfer for calculating the emergent spectrum from the disk is its optical depth in the infrared. For a torus with radial mass density profile $\rho = \rho_1 (r/R_1)^{-\alpha}$, the total cloud mass

$$M = 4\pi\theta_{\frac{1}{2}}\rho_1 R_1^3 f_\alpha, \quad (1)$$

where

$$f_\alpha = \frac{(R_2/R_1)^{3-\alpha} - 1}{3-\alpha} \quad (\text{for } \alpha \neq 3) \quad (2)$$

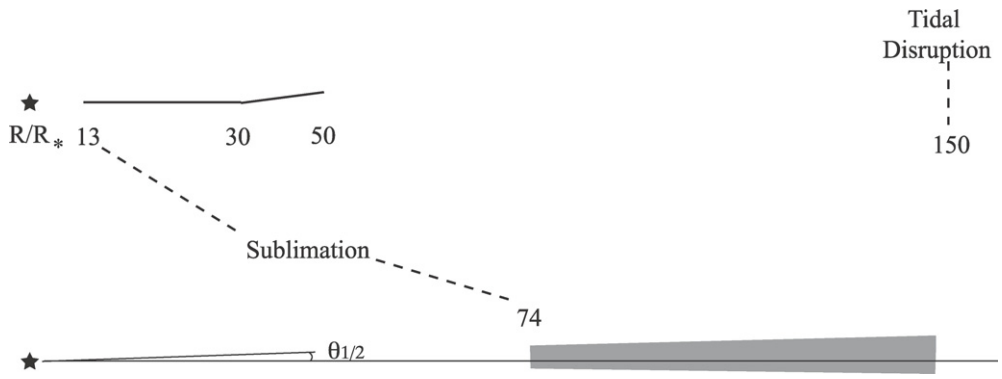

Figure 6. Cartoons illustrating possible geometries for the G29-38 disk. The physically thin plus warp model (top) is based on Jura's (2007) model for the similar white dwarf GD 362. The physically thick (bottom) is based on Reach et al. (2005a) and elaborated in Section 4. Distances from the star are labeled, in units of stellar radii. The distances from the star for grain vaporization (gray body grains at 1200 K) and tidal disruption (Roche limit for a solid body to be tidally disrupted by the white dwarf with radius 7.5×10^8 cm and mass 0.69 $M_\odot$) are indicated.

$$= \ln(R_2/R_1) \qquad (\text{for } \alpha = 3). \tag{3}$$

The vertical optical depth at the inner radius is

$$\tau_{\perp 1} = \frac{3 Q_{\rm IR} M}{16\pi \rho_d a R_1^2 f_\alpha}, \tag{4}$$

where a is the particle radius and $Q_{\rm IR}$ is the absorption efficiency averaged over the thermal emission spectrum. Using the cloud mass radius from Paper I ($R_1 = 1\ R_\odot$) and scaling the mass in units of 10^{18} g, $\tau_{\perp 1} = 0.03 M_{18} Q_{\rm IR} (a/\mu{\rm m})^{-1}$. For particles smaller than the wavelength, the absorption efficiency can be approximated as $Q_{\rm IR} \simeq 2\pi a/\lambda$, so the optical depth for thermal emission at wavelength λ is $\tau_{\perp 1,\lambda} = 0.2 M_{18} (\lambda/\mu{\rm m})^{-1}$, independent of particle size. For thermal emission at 10 μm, one can neglect radiative transfer out of the disk only if $M < 5 \times 10^{19}$ g.

Dust heating is determined by the propagation of starlight through the disk. The optical depth from the disk inner boundary to a distance twice as far from the star is

$$\tau_{\parallel 1} = \frac{\tau_{\perp 1} Q_{\rm opt}}{\theta_{\frac{1}{2}} Q_{\rm IR}} \frac{1 - 2^{-\alpha}}{\alpha - 1}. \tag{5}$$

For particles larger than 0.1 μm, $Q_V \simeq 1$ for absorption of starlight, and the optical depth from the star to the disk interior is $\tau_{\parallel 1} = 2.5 M_{18} (\theta_{\frac{1}{2}}/0.^\circ 8)^{-1} a_{\mu{\rm m}}^{-1} (R_1/R_\odot)^{-2}$. Using the mass and radius from Paper I, we find the cloud is optically thin for starlight propagation (and for thermal emission) as long as $\theta_{\frac{1}{2}} a_{\mu{\rm m}} > 2^\circ M_{18}$. The presence of the silicate emission feature further requires particle size less than 2 μm, so for a disk that is optically thin to propagation to starlight, we require $M_{18} < \theta_{\frac{1}{2}}$. The cloud must be at least as massive as derived in Paper I (where light was allowed to propagate through the disk unimpeded), so we finally obtain the constraint $1 < M_{18} < \theta_{\frac{1}{2}}$ for an optically thin disk. If the disk is more massive than the upper limit, it becomes optically thick to propagation of starlight, the temperature decreases more rapidly with distance from the star, and the cloud is more dominated by its inner edge. We will refer to this case as moderately optically thick, with $0.5 < \tau_\parallel < 10$ so the cloud is optically thin to vertical propagation of the observed infrared emission but optically thick to radial propagation of starlight (Section 4.1.2).

It appears therefore that a model cloud that is "physically thick" (i.e., thicker than the white dwarf's diameter) can still be quite flattened, with angular widths as small as 1°, before becoming optically thick. The distinction between the "physically thick" model (Reach et al. 2005a) and the "physically thin" model (Jura 2007) is that the physically thin model is thinner than the stellar diameter, so that it can be illuminated on its upper and lower surfaces. In order to intercept as much energy as is observed (3% of the white dwarf's luminosity), a physically thick model at its inner edge must have a half-width *at least* 10^9 cm, which is larger than the stellar radius ($\simeq 8 \times 10^8$ cm). Starlight does not illuminate the surface of the physically thick model, and instead the dust is heated by stellar photons that must propagate through the disk.

4.1.1. Spherical Shell Model

The simplest geometry for the cloud around G29-38, and a limiting case for the physically thick model, is a spherical shell. A moderately optically thick spherical shell will have the same temperature distribution as a disk with the same radial density variation. We use the spherical shell calculations to measure the radial temperature profile relative to the optically thin case.

Spherical shell calculations were performed using DUSTY[10] for a radial profile r^{-3}, an amorphous carbon or silicate composition, and a range of total optical depths, τ (at 0.55 μm), from 0.01 to 10. The inner boundary of the shell is where the dust temperature reaches 1100 K (fits with inner temperatures 1000 and 1300 K yielded significantly worse fits to the observed spectrum). Figure 7 shows emergent spectra compared to the observations. The first are visually very good, clearly reproducing the spectral shape, despite the simplicity of the model; however, the reduced $\chi^2_\nu = 2.2$ is statistically poor. The residuals are dominated by structure near the 9–11 μm silicate feature: the observed minus model residuals have positive peaks at 9.2 and 11.2 μm and a broad negative trough spanning 8–13 μm. The deficiencies of this model are thus due to using only one silicate, in contrast to the more detailed mineralogy found in the multi-composition models discussed above.

The luminosity of the shell per unit stellar luminosity is accurately approximated by

$$\frac{L_d}{L_*} \equiv f \simeq f_0 (1 - e^{-\tau}), \tag{6}$$

[10] Ivezic et al. (1999), User Manual for DUSTY, University of Kentucky Internal Report, accessible at http://www.pa.uky.edu/~moshe/dusty.

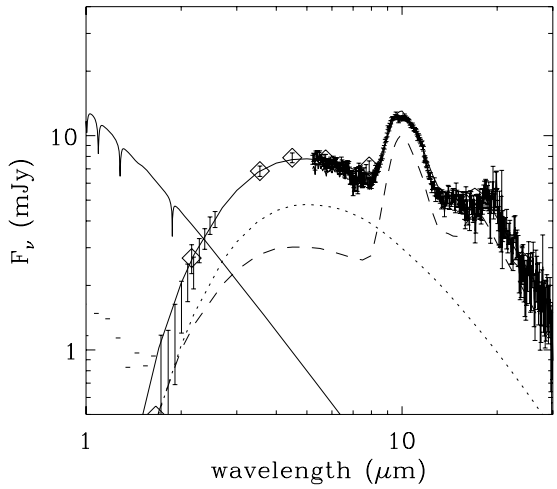

Figure 7. Spherical shell models for the dust around G29-38. Individual models for amorphous olivine and carbon are shown as dashed and dotted curves, respectively, and a linear combination is shown as the solid curve. The input white dwarf spectrum and the photosphere-subtracted infrared observations are shown for comparison. The DUSTY models have optical depth $\tau(0.55\ \mu\mathrm{m}) = 0.018$ and 0.011 in silicates and carbon, respectively.

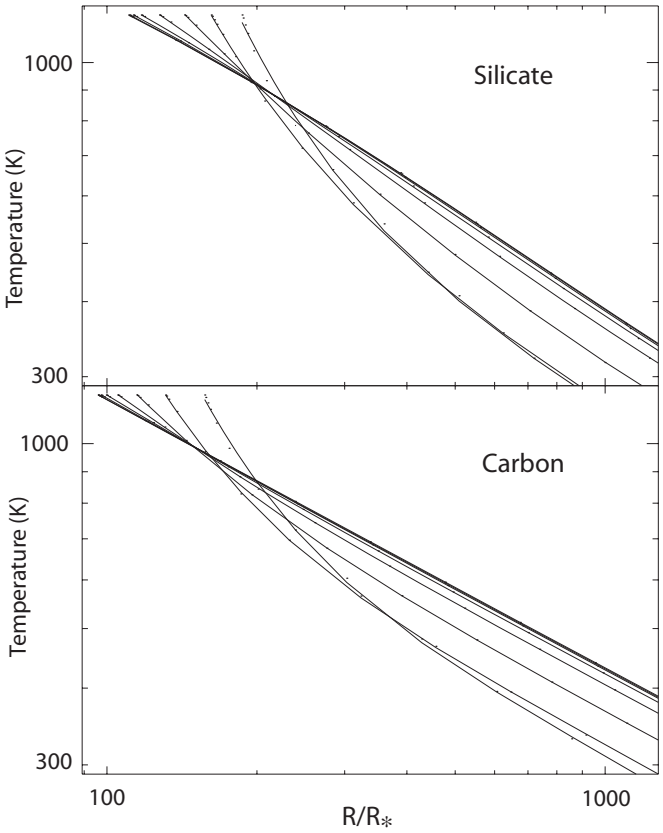

Figure 8. Temperature profiles in a spherical shell around G29-38. The top panel is for amorphous olivine, and the bottom panel is for amorphous carbon. All models are computed to an inner temperature of 1200 K. Each profile is for a different total optical depth, with values 0.0100, 0.0268, 0.072, 0.193, 0.518, 1.39, 3.73, and 10. The optically thin models extend closest to the star, are the warmest at the outer edge of the plot, and are closest to a straight line ($T \propto r^{-0.5}$). The optically thick models begin further from the star and decrease in temperature much more steeply.

where $f_0 = 0.74$ for carbon and 0.57 for silicate grains. The observed luminosity ratio, $f = 0.03$, could be explained by the combined carbon and silicate cloud from Figure 7 with optical depth at 5500 and 2000 Å of 0.028 and 0.044, respectively. The total extinction toward the star is small but could potentially be measured with precise UV/visible spectrophotometry, in which case the presence of carbonaceous grains could be tested by searching for a 2175 Å feature such as seen in the interstellar medium (Mathis 1994).

The temperature at a given distance from the star is the same for a spherical shell as for a moderately optically thick disk, as long as scattered light and dust thermal emission is a negligible heat source. Figure 8 shows the temperature profiles through shells with different optical depths. The temperature versus distance from the star for gray grains in the optically thin limit would follow $T \propto r^{-0.5}$. For real materials, and taking into account radiative transfer, the temperature profiles are significantly different. Using a power-law approximation $T \propto r^{-\delta}$, the predicted temperature profiles have $0.44 < \delta < 0.48$ as long as $\tau < 0.2$. But for higher τ a single power law is not adequate. We fitted the curves in Figure 8 with empirical functions for use in the moderately optically thick models. For reference, the temperature scalings are closely related to the parameter Ψ defined in the original paper on the self-similarity solution used in DUSTY (Ivezić & Elitzur 1997).

4.1.2. Moderately Optically Thick Model

Armed with the temperature profiles, and the wavelength-dependent cross-sections for each mineral, we can now compute the brightness of a flattened cloud that has optical depth $\tau_\parallel < 10$ and $\tau_\perp < 1$. We define this as a "moderately optically thick" disk. For simplicity we consider a fanned disk, with scale height proportional to distance from the star, $h = r \tan\theta_{\frac{1}{2}}$. The model does not apply to a thin, flat disk or a disk with a vertical density gradient. Full treatment of the optically thick disk with vertical density gradient requires a two-dimensional calculation that is beyond our present scope.

The moderately optically thick model was calculated for a subset of the minerals used in Section 3: amorphous carbon (Zubko et al. 1996), amorphous olivine (Dorschner et al. 1995), forsterite (pure-Mg crystalline olivine, Jäger et al. 2003), enstatite (pure-Mg crystalline pyroxene, Jäger et al. 1998), and bronzite (Fe-rich crystalline pyroxene, Henning & Mutschke 1997). Based on the results of Section 3, we expect the main constituents (in order) to be the amorphous silicates, carbon, and bronzite. Due to the moderately intensive computations and lack of in-hand UV–Far-IR laboratory data (required to span absorption of the white dwarf spectrum as well as thermal emission), we did not include as wide a range of minerals as in Section 3. For bronzite, we use the calculations for forsterite but scaled them by the relative small-particle emissivity over the range of wavelengths where the optical constants were available (6.7–500 μm). The most important compositions for which we did not calculate the moderately optically thick model were magnesium–iron sulfides, and water ice (which in fact cannot exist on grains in this model and requires a separate reservoir, as discussed in Section 3). The temperature of grains of each size (from 0.1 to 1000 μm) was calculated by balancing the radiation from the white dwarf, geometrically diluted by r^{-2} within $20 < r/R_* < 70{,}000$, with the grain's thermal emission. Figure 9 shows the grain temperatures for two materials and three particle sizes in this optically thin limit. The temperatures were then adjusted using the scale factors derived in the previous section appropriate for the composition, the distance from the star, and the total cloud optical depth. If a grain's temperature

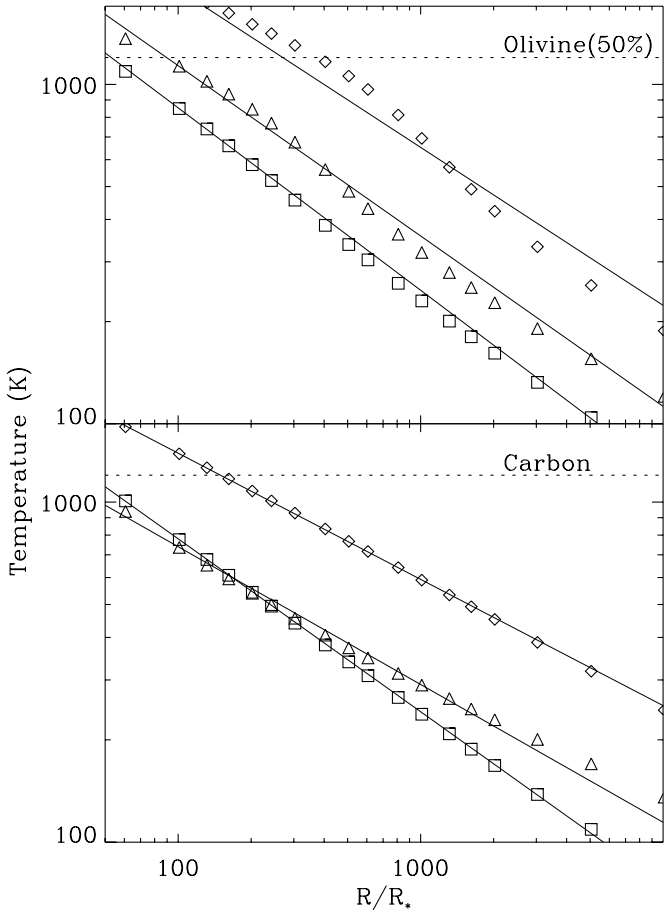

Figure 9. Temperatures of olivine (top) and carbon (bottom) grains of three different sizes: 0.1 μm (diamonds), 1 μm (triangles), and 10 μm (squares). The grains are irradiated directly by the white dwarf (i.e., the cloud is optically thin). The solid line shows power-law fits of the form $T = T_1(r/100R_*)^{-\delta}$. For olivine (carbon) grains of 0.1, 1, and 10 μm radius, $T_1 = 1905$, 1136, 853 K (1393, 740, 780 K), and $\delta = 0.47$, 0.50, 0.54 (0.37, 0.41, 0.51), respectively. The horizontal dotted line indicates the vaporization temperature (1200 K) in our model.

exceeds a vaporization temperature, $T_{\rm vap}$, its emissivity is set to zero. Values of the vaporization temperature in the 1000–2000 K range are expected for most minerals; evidence for inner edges of YSO disks at distances corresponding to these vaporization temperatures has been found in interferometric observations (Monnier & Millan-Gabet 2002). The emission spectrum of dust at each distance from the star was calculated by integrating over several size distributions: a power law $\propto a^{-3.5}$, a Hanner law with slope 3.7 and critical size 7.4 μm, the size distribution from the coma of comet Halley, and the size distribution of interplanetary meteoroids and lunar microcraters (Grün et al. 1985).

The emergent spectrum from the cloud was then calculated by integrating in spherical coordinates using a radial density distribution $n \propto r^{-\alpha}$ and minimum radius $R_{\rm min}$, with individual models sampled from the ranges $0.3 < \alpha < 6$ and $50 < R_{\rm min}/R_* < 1000$. We assume azimuthal symmetry and optically thin infrared emission, so the opening angle of the disk $\theta_{\frac{1}{2}}$ does not affect the spectral shape. A range of $1000\,{\rm K} < T_{\rm vap} < 1600$ K and $0 < \tau_{\|} < 10$ were considered. Then for each cloud geometry (α, $R_{\rm min}$), a linear combination of the models for carbon, olivine, and forsterite was fitted to the observations, and the χ^2 for the mixture computed. Because these materials

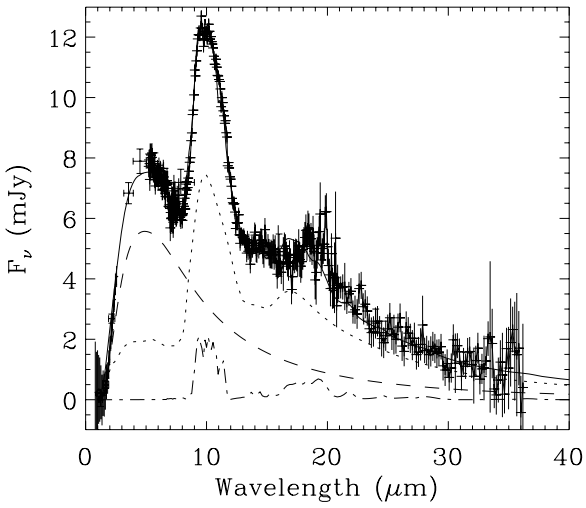

Figure 10. Best-fitting moderately optically thick disk model (solid line) combining amorphous carbon (dashed), amorphous olivine (dotted), crystalline bronzite (dash-dot) to the observed photosphere-subtracted spectral energy distribution of G29-38.

Table 4
Best-Fitting Moderately Optically Thin Model

Parameter	Best Value	Confidence Interval
$T_{\rm vap}$	1100 K	1050–1200 K
$\tau_{\|}$	2	1–8
$R_{\rm min}$	50	$\leqslant 150$
α	2.7	2.4–2.9

vaporize at $R < 50R_*$ for essentially all particle sizes (see Figure 9), all models with $R_{\rm min} < 50R_*$ are equivalent.

The best-fitting solution is enumerated in Table 4 and illustrated in Figure 10. Given 390 data points in the spectral energy distribution, we expect a "good" fit to have reduced $\chi^2_\nu \simeq 1$ within dispersion $\sqrt{2/390} = 0.07$. The best-fitting model had $\chi^2_\nu = 1.23$. We discuss the residuals, which are localized rather than spanning a wide wavelength range, in the following paragraph; for statistical purposes, we assume they are unrelated to the cloud geometry. The confidence intervals for the parameters, determined by $\Delta\chi^2_\nu = 0.07$, are listed in Table 4.

The residuals from the radiative transfer model are shown in Figure 11. Coherent features dominate the residuals; the amount by which they increase χ^2_ν measures their statistical significance. These include the following: (1) a "W"-shaped pattern between 8 and 10.5 μm ($\Delta\chi^2_\nu = 0.30$); (2) an "S"-shaped pattern between 15 and 21 μm ($\Delta\chi^2_\nu = 0.24$); and (3) a "U"-shaped residual between 1 and 3 μm ($\Delta\chi^2_\nu = 0.20$). Each of these features is statistically significant. Feature (1) is due to mismatching the fundamental silicate Si–O stretch feature; an additional silicate is required which provides a shorter-wavelength silicate feature than Mg-rich olivine. Feature (2) is due to either mismatching the silicate Si–O–Si bending feature or the presence of MgO (or $Mg_xFe_{1-x}O$ with $x > 0.5$), which has a peak at 18.5 μm. Cosmic abundances favor formation of Mg-rich silicates over Mg oxides, so a preferable solution for residual features (1) and (2) is a silicate with bluer fundamental and better matching Si–O–Si bending mode features.

We experimented with the following minerals, inspired by the results of Section 3. All models included amorphous carbon and olivine. Additional (third) minerals were included one at a time; the most successful were bronzite ($\chi^2_\nu = 1.22$) and

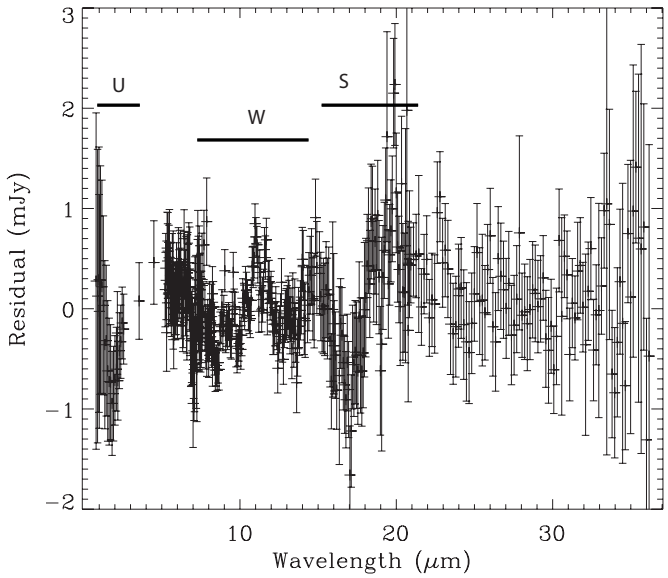

Figure 11. Residuals (observed minus model) from the best-fitting moderately optically thick disk model of Figure 10. Features discussed in the text are labeled.

forsterite ($\chi^2_\nu = 1.55$), in order of goodness of fit. These results are consistent with those in Section 3, where an Fe-rich pyroxene was shown to be the third most important mineral. Then for the most successful third minerals, fourth minerals were added; a good combination was forsterite plus montmorillonite ($\chi^2_\nu = 1.23$), but it was only slightly better than the bronzite model alone. Other minerals such as amorphous pyroxene yielded negligible improvement to the fit ($\Delta\chi^2_\nu = 0.02$). The materials commonly referred to as amorphous olivine and amorphous pyroxene are both amorphous silicates and are essentially indistinguishable. It appears to be significant that Fe-rich pyroxene is more abundant than Mg-rich olivine; this is directly due to Fe-rich pyroxene having a bluer fundamental Si–O stretch (as observed) compared to forsterite. From the laboratory measurements of phyllosilicates by Glotch et al. (2007), there are two properties that make them possible explanations for residual features (1) and (2): phyllosilicates have an Si–O stretch that is bluer than forsterite, and they have a double-peaked Si–O–Si bending mode that is similar to the shape observed in the G29-38 spectrum from 18 to 20 μm.

The distinction between the bronzite model and the forsterite + montmorillonite model is mathematically within the errors, but we will refer primarily to the former model since it is simpler and agrees with the more extensive mineral search from Section 3. The fit could be improved if a more exhaustive mineral search were performed. However, the results of Section 3 already demonstrate that including a wide range of minerals can explain the silicate feature shape adequately, and we are already at a reduced $\chi^2_\nu = 1.2$ so that the present S/N does not allow further, unique modeling.

Feature (3) in the residuals relates to the shape of the inner edge of the disk and the vaporization temperature. We only explored $T_{\rm vap}$ on a grid with 100 K intervals, and fixed it at the same value for all compositions, so the observed, modest deviations from our model are not particularly surprising in the near-infrared. Further, we did not explore the composition of the featureless materials, which could affect not only their $T_{\rm vap}$ but also the slope of their absorption around 3–6 μm, which determines the shape of the inner edge of the disk spectrum.

4.2. Physically Thin Disk

A physically thin disk is very *optically* thick, so starlight cannot propagate radially through the disk. Such a disk must be so thin that the star can illuminate its surface, or it must be warped such that the surface has clear lines of sight to the star, or a combination of both effects as described by Jura (2007). The temperature versus distance from the star scales as $r^{-0.75}$ (e.g., Chiang & Goldreich 1997). The flux from an optically thick disk is straightforward to estimate: for G29-38, the disk temperature $T = 8008(R/R_*)^{-0.75}$ K, and the stellar radius $R_* = 8 \times 10^8$ cm, so the model is determined only by the inner and outer radii of the disk. If we furthermore set the inner radius to be that at which dust sublimates, the only free parameter is the outer radius of the disk. Since emission from the inner radius dominates at the shortest wavelengths, the optically thick model makes robust predictions of the disk flux at the wavelength where emission from material at the vaporization temperature peaks, i.e., around 3 μm. The flux at longer wavelengths depends on the outer radius.

As observed from Earth, the disk may of course be inclined with respect to the line of sight (von Hippel et al. 2007), though previous calculations considered face-on geometry for illustration (Jura 2003, 2007). The flux will scale as $\cos i$, where i is the angle between the disk axis and the line of sight, until $i \rightarrow \tan^{-1} H/R_{\rm outer}$, where $R_{\rm outer}$ is the outer radius of the disk and H is its scale height. Taking the outer radius $\sim 50R_*$ from the GD 362 model (Jura 2007), and requiring disk thickness $H < R_*$, the low-inclination limit only applies when $i < 1\overset{\circ}{.}2$. The nearly edge-on limit is relatively improbable and furthermore would cover the star unless $H \ll R_*$, in which case the edge-on limit applies to even less probable geometries. An optically thick disk has a spectral energy distribution determined almost entirely by the outer radius, and total flux scaling with $\cos i$.

Using the *Spitzer* spectra, it is clear the simple optically thick model is definitively ruled out by the presence of a very strong silicate emission feature: this feature requires an optically thin emitting region. The feature contributes a significant portion of the disk luminosity and must have associated continuum. Further, the observed spectral energy distribution requires a colder component with color temperature $\sim$ 290 K (Reach et al. 2005a) to explain the flux at 24 μm. As a first step toward constraining a possible optically thick disk around the star, we fitted the thin-disk model to the spectrum excluding the silicate feature (8–12 μm) and setting the inner radius as the location where the grain temperature is 1200 K. The best fit has $\chi^2_\nu = 3.8$; this high value is due to the lack of significant emergent cold flux from the model. However, we take the constraints on R_2 and i as a guide, with best values $R_2/R_* = 49 \pm 5$ and $i = 41^\circ \pm 3^\circ$.

Instead of attempting to fit the entire spectrum with the thin-disk model, we now consider only fitting it to the shorter-wavelength continuum, with an eye toward adding a cooler, physically thick silicate-bearing cloud. Thus, we excluded wavelengths longer than 8 μm and fitted the physically thin model to the spectrum of G29-38. The near-infrared spectrum and the decrease from 5 to 8 μm require that the inner edge of the disk is closer to the star than the point that reaches 1200 K; a better fit is obtained with $T_{\rm vap} = 1500$ K so that $R_1 = 9R_*$. Figure 12 shows the constraints on outer radius (R_2) and inclination (i). The best fit has a low $\chi^2_\nu = 0.8$; it is probably less than 1 due to overestimation of the uncertainties due to photospheric subtraction in the near-infrared. The best-fitting outer radius is $R_2 = 25R_*$ and the inclination is 23°. It is notable

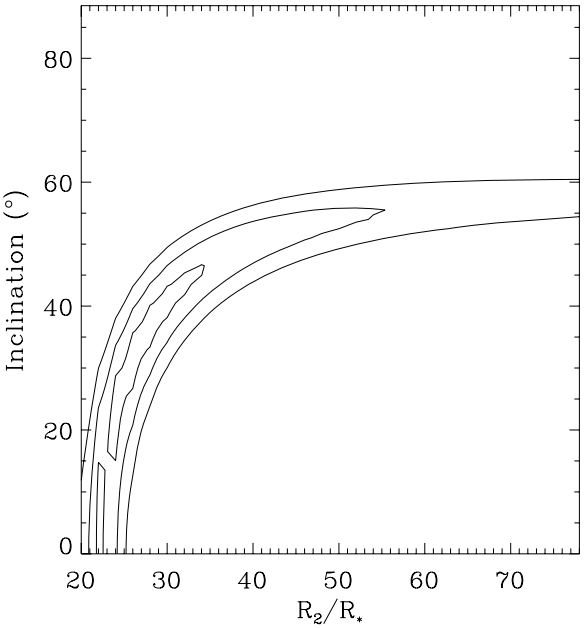

Figure 12. Goodness of fit (χ^2/dof) from the physically thin, optically thick model for a range of outer radii (R_2, in units of stellar radius) and inclination. The best-fitting model has inner and outer radii $R_1 = 9$, $R_2 = 25$, and inclination 23°.

that the required inclination is roughly in the range required by Graham et al. (1990) in his model for the near-infrared timing (which required an inclination such that the dust temperature pulsations are detectable while the exciting pulsations on the photosphere are not).

An amendment to the physically thin disk model is needed to improve the fit and explain the silicate emission. One possible solution is to include an optically thin, effectively physically thick region at the outer edges of the ring. Jura (2007) showed that for GD 362, an extension of the ring that is warped by only $\sim 7°$ can produce a silicate feature in emission. Figure 6 shows their model, compared to the moderately thick model from Section 4.1.2. Indeed this outer region produces both the silicate feature and a significant fraction of the continuum at $\lambda > 11$ μm in their model. The plausibility of the warp of the outer disk is discussed and justified physically by Jura (2007), who label it as "region III" in their model. In many ways, the details (mass, temperature, radius, vertical extent) of this outer portion of the disk must be similar to the physically thick model, since they explain the mid-infrared emission in the same way (an optically thin cloud of silicates). In the warped disk model, the optically thin region is actually the upper layer of the disk; i.e., even the warped portion of the disk may be optically thick, as long as it has a direct line of sight to the star.

4.3. Comparing the Thick and Thin Models

The disk spectral energy distribution can be empirically decomposed into three major components. One of them is a continuum with a relatively hot (890 K) color temperature, peaking around 4 μm and dominating the near-infrared emission. Another component is continuum with a lower color temperature ($\sim$ 300 K). The other major component is the silicate emission feature. In the Jura (2007) model, the hot component is the blackbody disk—hot because it is close to the star—and the cooler continuum and silicate feature arise in the outer warp region III. In the physically thick model (in Paper I and Section 4.1.2),

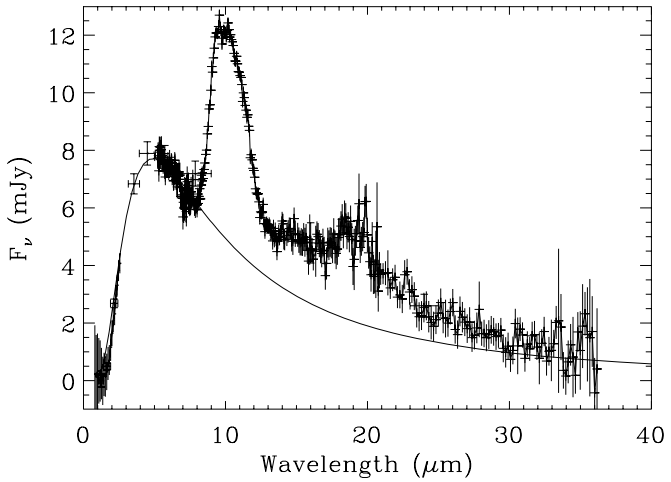

Figure 13. Best-fitting physically thin, optically thick disk model. The model (solid line) was only fitted to data at wavelengths less than 8 μm; it cannot produce the silicate feature and underpredicts (by far) the longer-wavelength continuum.

the hot component is amorphous carbon (hot because it is due to highly absorbing material), and the cooler component is silicates (cool because the silicates are more transparent and have strong mid-infrared emission features that allow them to cool efficiently); the two materials are colocated.

For many plausible configurations of solid material around the white dwarf, we can consider the cloud as the sum of an optically thick disk and an optically thin halo or flared disk surface. Indeed, Vinković et al. (2003) proved mathematically that flared disk models are equivalent to disk plus halo models. The radial profile of a spherical halo can be directly related to the flaring angle of a flared disk. Thus, it is not possible, using the spectral energy distribution alone, to separate disk and halo (or warped disk) models. The halo dominates the infrared emission when $\tau_{\rm halo} > H/4R$, where H is the flare height and R is the distance from the star (Vinković et al. 2003). For the wedge-shaped "physically thick" model discussed above, this is equivalent to $\tau_{\parallel} > \tan\theta_{\frac{1}{2}}/4$. Equating the emission and absorbed flux (3% of the stellar flux), the halo will dominate the infrared emission when $\tau_{\parallel} > 0.004$, which is already required for both the physically thick and thin models.

For the specific case of the G29-38 disk, we made a direct substitution of the optically thick disk for the C/Fe component of the moderately optically thick model. The optically thick disk was taken directly from the model in Figure 13 (i.e., the one fitted to wavelengths shorter than 8 μm), and the silicate components were taken from the moderately optically thick model in Figure 10. The silicate component of the moderately optically thick disk was rescaled in amplitude in order to match the observed flux after being added to the optically thick disk. The parameters for the best-fitting disk in this combined disk+silicate model are similar to those derived above using only short-wavelength data: $R_2 = 22R_*$ and $i = 29°$. Figure 14 shows the best fit; it is very similar to the moderately optically thick model in Figure 10; the goodness-of-fit, $\chi^2_\nu = 1.40$, not much worse than the moderately optically thick model. Improvements to χ^2_ν as obtained in Section 3 could be obtained by including more minerals in the optically thin region.

5. TIMING CONSTRAINTS

The geometry of the G29-38 disk can be constrained using timing information. The star is a ZZ Ceti variable with

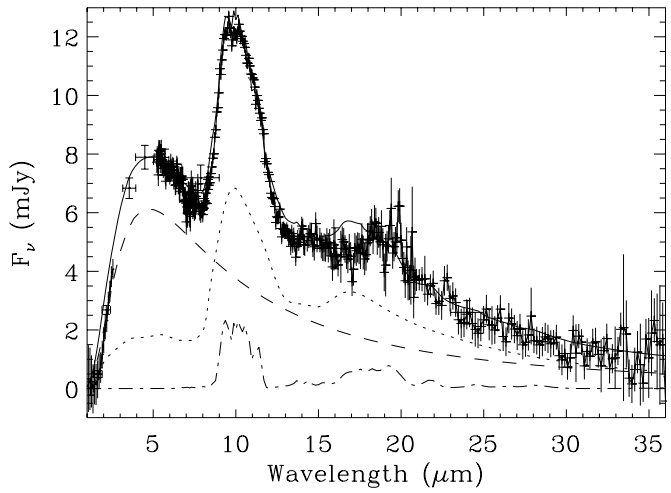

Figure 14. Best-fitting combined model, with a physically thin, optically thick disk (see Figure 13) plus a silicate-only (no C or Fe) physically thick disk (see Figure 10).

nonradial modes that yield its optical pulsations. Graham et al. (1990) found pulsations at periods $\sim$ 200 s in the *K* and *L* bands that have no strong counterpart in *J* and *B* bands. More detailed optical photometry clearly shows pulsations at the predicted frequency: see the peak around 5380 μHz from the Whole Earth Telescope observations (Winget et al. 1990). The weakness of this mode at visible wavelengths compared to infrared wavelengths could be due to the manner in which it interacts with the disk. The *B*-band light is completely dominated by direct photons from the star, while the *K*-band light contains a contribution from thermal emission by the dust that produces the mid-infrared excess. The *K*-band pulsations are attributed to dust temperature variations.

As Graham et al. (1990) explained, to generate observable *K*- and *L*-band pulsations from a mode that is not prominent on the photosphere, the geometry is constrained. They invoke a mode of stellar brightness variations (second-order spherical harmonic) that brightens the pole and dims the equator of the star. If the disk is thin enough that its heating is driven by the equatorial stellar brightness, then it will track the equatorial photospheric temperature, rather than the average over the surface. Graham et al. (1990) show that the spherical harmonic that excites the disk temperature variations can exist without significant variation of optical wavelength light if the star is viewed at the angle where the ratio of the two spherical harmonics is small. To eliminate the *J*-band variability in their data required a viewing angle in the range 45°–65°.

The IRAC observations confirm the significance of the 200 s period in the near-infrared. (No modes with periods longer than 500 s are detectable due to the brevity of the IRAC observations, so we could not address the 615 s period that dominates the optical pulsations; Winget et al. 1990.) The fluctuating portion of the infrared flux, after subtracting the direct stellar photosphere, is 7% at 2.2 μm, 5% at 3.6 μm, and less than 3% at 8 μm. The color of the fluctuations suggests that they arise from the inner portion of the disk, near the dust vaporization temperature. This explanation works well with the physically thin disk model with the inner edge of the disk at 1200 K and decreasing temperature outwards. The timing constraints rule out a spherical distribution for all the dust, though some dust can remain in a spherical distribution without generating pulsations (because the temperature variations average out over a sphere). The observations do not yet rule out a "physically thick" configuration with a small opening angle ($\theta_{\frac{1}{2}}$). We consider the Graham et al. (1990) results very important; they require observational confirmation and have the promise of revealing the disk structure in more detail.

6. DISCUSSION AND CONCLUSIONS

The mid-infrared spectrum of G29-38 is due to a cloud of small particles orbiting the star within the distance where tidal forces from the white dwarf's strong gravity would destroy a large, weak body. The tidal forces exceed the self-gravity and strength of a nonrotating, rigid spherical body within a distance

$$d/R_* = 120\rho^{-1/3}\left[1 + 0.11\frac{S_{\rm kPa}}{\rho r_{10}^{-2}}\right], \quad (7)$$

where ρ is the bodies density (g cm^{-3}), r_{10} is its radius (in units of 10 km), and $S_{\rm kPa}$ is its strength in kPa. If the dust around G29-38 was produced by one body, then the present-day mass requires $r_{10} > 1$. For an asteroid or comet, we expect $0.5 < \rho < 2$. Spin rates of near-Earth objects require strengths $\sim 2r_{10}^{-1/2}$ kPa to balance centrifugal forces against strength (Holsapple 2007). The strength term in Equation (7) is thus negligible for bodies with $r_{10}\rho > 1$, which is likely for the parent bodies of G29-38 dust. Fragments of parent bodies can survive much closer to the star; rocks with $S_{\rm kpa} = 3000$, $\rho = 3$, and could survive against tidal disruption all the way to the surface of the star if they are smaller than 0.1 km.

In the spectrum of G29-38, the strong emission feature at 9–11 μm, the color temperature, and the timing information all support the interpretation of the mid-infrared excess as being dominated by a cloud of small silicate particles. The infrared excess at 2–6 μm is apparently due to a featureless blackbody continuum. Based on our modeling results, this high-color-temperature emission could be explained either by a highly absorbing mineral (like solid C or Fe) or by a massive disk of material that is thinner than the white dwarf's diameter. The difference between these models, both of which can explain the observed spectral energy distribution reasonably well, is significant: the massive disk model could harbor 10^{24} g (or more) of dust (Jura 2003), while the cloud of amorphous C or Fe requires $\sim 10^{19}$ g. There is no a priori reason that either of these mass estimates should be preferred or rejected. Some 10^{19} g of silicates are required in all models.

To understand the origin of the circumstellar material, it is important to know how much mass is observed. If only 10^{19} g of material is present, then the observed infrared excess can be explained by a single small asteroid or a comet. If 10^{24} g of material is present, then an entire, large asteroid, or numerous smaller ones, is required. In all cases, the parent body must have been somehow transported from a distance far enough from the star that it could have survived the red giant and AGB phase of the star (greater than 5×10^{13} cm) inward to the Roche limit where it would be disrupted by the gravity of the white dwarf (less than 10^{11} cm).

6.1. Nature of the Parent Bodies

The mineralogical results can help us relate the dust to possible parent bodies. We concentrate on the two primary components of the spectrum separately: the silicate material (required in all models in order to explain the 9–11 μm emission

feature) and the highly absorbing material (required only in the thick-disk models).

The composition of the highly absorbing material cannot be determined unambiguously from the spectrum. We fitted it in Section 3 with amorphous C, based on the high cosmic abundance of C. But solid Fe or Si are also plausible, given their high cosmic abundance. Indeed, for chondritic (asteroidal and terrestrial) material the abundance of Si and Fe is much higher than C (Jura 2006). Mineralogical models for dust around other stars and in comets, using the same methodology as in Section 3, do not always show a high abundance of C (Lisse et al. 2007a, 2007b). For extrasolar systems, a careful subtraction of the photosphere is critical to measuring the high-color-temperature emission (which is characteristic of highly absorbing material like solid C). For G29-38, the high-color-temperature excess (at 3.6 μm and longer wavelengths) is so far above photosphere that it must arise from circumstellar material, but at wavelengths shorter than 2 μm the infrared excess shape depends on the photosphere model. For G29-38 the mid-infrared data clearly require emission with a color temperature greater than 800 K, whether it is C or Fe.

The compositions of the potential parent bodies for the circumstellar material around white dwarfs can be addressed by studies of solar system bodies. To date there has been no sample return mission from an asteroid, but meteorites provide direct measures of composition of parts of at least some asteroids. Carbonaceous chondrites have some C, but all chondrites are largely silicate mineral (olivine and pyroxene, mostly Mg-rich (forsterite and enstatite)), with a wide range of other minerals (some Ca- and Al-rich) and metals (often including previously molten Fe). Metallic meteorites, commonly found in museums and on the ground, have largely Fe and Ni composition (Shearer et al. 1998). Comets are likely to have a more primitive composition than carbonaceous chondrites, with abundant silicate grains as well as carbonaceous material, based on the infrared spectroscopy of cometary dust, laboratory study of cometary interplanetary dust particles, and in situ mass spectrometry during the 1P/Halley flyby in 1986 (Hanner & Bradley 2004). The most abundant silicate minerals in meteorites are Mg-rich olivines and pyroxenes, as well as feldspar and phyllosilicates. Interplanetary dust particles believed to originate from comets (CP type) are largely composed of phyllosilicates that require aqueous alteration on their parent body (Messenger et al. 2006).

Based on the analogy to solar system bodies, the dominance of Fe-rich pyroxene mineralogy is distinct. Comets or outer-main-belt (D-type) asteroids contain Mg-rich olivine and phyllosilicates, which when combined can reasonably fit the observed spectrum of G29-38. Both comets and D-type asteroids contain organic material, which would be consistent with the presence of amorphous C, and the most primitive carbonaceous (CI) meteorites are largely composed of phyllosilicates. But the Mg-rich olivine plus phyllosilicate model is not as good a fit to the data as Fe-rich pyroxene. There are pyroxene-dominated meteorites, but they are dominated by Mg-rich pyroxene (hence the name enstatite meteorites for this rare class). It is worth noting that enstatite chondrites are thought to have formed in reducing conditions and contain other minerals including niningerite (Weisberg et al. 2006), which was one of the most abundant minerals from our fit for G29-38 in Table 3. Thus, the physical conditions for the formation of the enstatite meteorite parent bodies may have some relevance to the formation of the G29-38 debris parent body.

In terms of the featureless material that produces the near-infrared continuum (in the physically thick models), either C or Fe are acceptable to the fits. If the material were C, then a cometary or D-type asteroid origin would be more likely, whereas with abundant Fe, formation closer to the star and within a differentiated parent body would be implicated.

Some constraints on the composition of the material are obtained from the abundances in the white dwarf atmosphere. Solid material at the inner edge of the disk is constantly being vaporized by the stellar radiation. These vapors reach the atmosphere of the star (or are blown out of the system). They cannot reside in the stellar atmosphere for long; instead, they diffuse rapidly inward, deeper than the photosphere. Thus, the heavy elements in the stellar atmosphere must be "fresh," consistent with an origin from vaporization of circumstellar dust but not with a long-lived stellar atmosphere. G29-38 has metals present in its atmosphere. Jura (2006) discussed the deficiency of C in some externally polluted white dwarfs, where the abundance of C relative to Fe is more than 10 times lower than solar. CI meteorites have C/Fe 10 times lower than solar; this is commonly explained by the volatility of C and the high temperature required for chondrite formation (Brearley and Jones 1998). We note that the abundances of refractory elements in comets *and* asteroids as well as that inferred from exozodiacal dust is consistently less than solar, in the 7%–10% range (Lisse et al. 2006). But in a relative abundance, dust collected during the encounter with the long-period comet 1P/Halley has C/Fe abundance ratio similar to solar (Jessberger et al. 1988). Short-period comets (which are periodically heated to higher temperature) may be more devolatilized and may have abundances more similar to asteroidal material.

6.2. Disruption of "Hot Jupiter"?

One intriguing possibility for the origin of the infrared excess is the survival of the core of a giant planet and its subsequent gravitational disruption. "Hot Jupiters," with masses of order 10^{30} g orbiting within 10^{12} cm (0.1 AU) of their star, appear to be fairly common in extrasolar planetary systems: 1.2% of nearby F, G, and K stars have such a planet (Marcy et al. 2005). In this scenario, the planet would become engulfed into a common atmosphere during the red giant phase. Drag from the extended stellar atmosphere would cause the planet to spiral inward toward the stellar core. At the end of the mass-losing phase of the star's evolution, we would be left with a white dwarf, the surviving core of the planet, and the planetary nebula composed of the outer atmosphere from the star.

If a planet began at less than 10^{12} cm from the star, it is possible that its remnant could land within the Roche radius. The effect of the post-main-sequence evolution on the planetary dynamics has not been explored in detail. The change in mass of the central star could make any borderline-unstable system of multiple planets unstable (Debes & Sigurdsson 2002) and could lead to nonlinear orbital perturbations. A simple estimate of the orbital decay due to gas drag when the planet is within the red giant atmosphere is made by setting the rate of kinetic energy imparted to the planet,

$$\dot{E} = \frac{1}{2}\rho\pi R_p^2 \left(\frac{GM_*}{a}\right)^{3/2}, \quad (8)$$

equal to the change in the orbital binding energy

$$\dot{U} = \frac{GM_*M_p}{a^2}\frac{da}{dt}, \quad (9)$$

where M_p and R_p are, respectively, the mass and radius of the planet, G is the gravitational constant, a is the semi-major axis of the presumed circular orbit, M_* is the mass of the star, and ρ is the mass density of the star at the distance of the planet. Taking for illustration a planet with the mass of Jupiter and average density 1 g cm^{-3}, orbiting at a distance of 0.1 AU from a star of mass 2 $M_\odot$ that has mass density 10^{-9} g cm^{-3} at 0.1 AU from its center, the timescale for orbital decay is 6×10^4 yr. This is much smaller than the AGB lifetime $\sim 10^7$ yr (Vassiliadis & Wood 1993) for a progenitor star mass of 3.1 $M_\odot$ (Weidemann 2000). Thus, the inward spiral of hot Jupiter (or other close-in) planetary orbits is likely to be rapid, once the star has entered its giant phase.

Considering only a convective main-sequence primary star, Sasselov (2003) showed that the orbit of a "hot Jupiter" like OGLE-TR-56b would tidally decay on a timescale of 1–10 gyr. Again considering only a main-sequence primary star, Baraffe et al. (2004) showed that planets with masses less than 3×10^{30} will evaporate down to a rocky core in less than 5 gyr. These effects may combine, with tidal decay enhancing evaporation (Erkaev et al. 2007). The tidal decay of "hot Jupiter" orbits cannot be too rapid for main-sequence stars, or else they would be much less common. The orbital evolution is very sensitive to the stellar structure and the planet's orbital eccentricity; the response is highly nonlinear and may lead to a rapid inward spiral upon perturbation of the stellar interior structure or eccentricity (Ogilvie & Lin 2007; Jackson et al. 2007). Nonetheless, regardless of whether tidal decay can bring planets close to the stellar surface during main-sequence evolution, the gas drag during the red giant phase should finish the job.

How much of a "hot Jupiter" could survive the late stages of its star's evolution is not known. A brown dwarf was recently discovered around a white dwarf suggesting that some companions can survive the red giant phase of the primary star despite being well within the atmosphere (Maxted et al. 2006). Indeed, the companion is within the Roche distance of the white dwarf unless it has a mass density greater than 3.6 g cm^{-3} or is held together by more than its own gravity. The composition of the core of an extrasolar giant planet is difficult to constrain. Mass and radius estimates seem to require a dense core, possibly of high-pressure ice or stony composition (Burrows et al. 2007). This material would be tidally disrupted, as in the asteroid (or comet) disruption models considered to date. The Fe-rich pyroxene mineralogy for the G29-38 debris, which is distinct from that of most comets and asteroids, does not appear impossible for a rocky planetary core, but at present there is little more than can be said about whether such a mineralogy is likely.

That G29-38 is exceptional among debris disks (having by far the brightest infrared excess, with 3% of the star's luminosity absorbed and radiated by dust) makes the hypothesis more attractive. Consider the reverse argument: if 1% of all stars have "hot Jupiters," what is their expected end state? From this point of view, it seems inevitable that such remnant planets would generate debris for their parent star in its white dwarf phase. But this argument assumes that "hot Jupiters" exist around A-type stars (the progenitor type for G29-38), at least part of the planet can survive the common envelope phase, the remnant core lands within the Roche radius, and the debris can survive 500 Myr (the age of G29-38). The age problem may not be severe if the remnant planetary core becomes fragmented, with fragments gradually entering the Roche radius due to collisional disruption and gravitational perturbations. Further theoretical work is needed to test the viability of this scenario.

W.T.R. gratefully acknowledges discussions on radiative transfer in disks with Moshe Elitzur in 2007 May. W.T.R. gratefully acknowledges discussions on extrasolar giant planets with Adam Burrows in 2007 June. This work is based in part on observations made with the *Spitzer Space Telescope*, which is operated by the Jet Propulsion Laboratory, California Institute of Technology under NASA contract 1407.

REFERENCES

Backman, D. E., & Paresce, F. 1993, in Protostars and Planets III, ed. E. H. Levy & J. I. Lunine (Tucson, AZ: Univ. Arizona Press), 1253
Baraffe, I., Selsis, F., Chabrier, G., Barman, T. S., Allard, F., Hauschildt, P. H., & Lammer, H. 2004, A&A, 419, L13
Beichman, C. A., et al. 2006, ApJ, 639, 1166
Bergeron, P., Wesemael, F., & Beauchamp, A. 1995, PASP, 107, 1047
Bradley, J. P. 2002, Highlights Astron., 12, 34
Brearley, A. J., & Jones, R. H. 1998, Rev. Mineral. Geochem., 36, 301
Bryden, G., et al. 2006, ApJ, 636, 1098
Burrows, A., Hubeny, I., Budaj, J., & Hubbard, W. B. 2007, ApJ, 661, 502
Chen, C. H., et al. 2006, ApJS, 166, 351
Chiang, E. I., & Goldreich, P. 1997, ApJ, 490, 368
Chihara, H., Koike, C., Tsuchiyama, A., Tachibana, S., & Sakamoto, D. 2002, A&A, 391, 267
Debes, J. H., & Sigurdsson, S. 2002, ApJ, 572, 556
Dohnanyi, J. W. 1969, JGR, 74, 2531
Dorschner, J., Begemann, B., Henning, T., Jaeger, C., & Mutschke, H. 1995, A&A, 300, 503
Durda, D., & Dermott, S. F. 1996, Icarus, 130, 140
Edoh, O. 1983, PhD thesis, Univ. Arizona
Erkaev, N. V., Kulikov, Yu. N., Lammer, H., Selsis, F., Langmayr, D., Jaritz, G. F., & Biernat, H. K. 2007, A&A, 472, 329
Fazio, G. G., et al. 2004, ApJS, 154, 10
Glotch, T. D., Rossman, G. R., & Aharanson, O. 2007, Icarus, 192, 605
Graham, J. R., Matthews, K., Neugebauer, G., & Soifer, B. T. 1990, ApJ, 357, 216
Greenstein, J. L., & Liebert, J. W. 1990, ApJ, 360, 662
Grün, E., Zook, H. A., Fechtig, H., & Giese, R. H. 1985, Icarus, 62, 244
Hanner, M. S., & Bradley, J. P. 2004, in Comets II, ed. M. C. Festou, H. U. Keller, & H. A. Weaver (Tucson, AZ: Univ. Arizona Press), 555
Henning Th., & Mutschke, H. 1997, A&A, 327, 743
Holberg, J. B., & Bergeron, P. 2006, AJ, 132, 1221
Holsapple, K. A. 2007, Icarus, 187, 500
Houck, J. R., et al. 2004, ApJS, 154, 18
Ivezić, Ž., & Elitzur, M. 1997, MNRAS, 287, 799
Ivezić, Ž., Nenkova, M., & Elitzur, M. 1999, arXiv:astro-ph/9910475
Jackson, B., Greenberg, R., & Barnes, R. 2008, ApJ, 678, 498
Jäger, C., Dorschner, J., Mutschke, H., Posch, Th., & Henning, Th. 2003, A&A, 408, 193
Jäger, C., Molster, F. J., Dorschner, J., Henning, Th., Mutschke, H., & Waters, L. B. F. M. 1998, A&A, 339, 904
Jessberger, E. K., Christoforidis, A., & Kissel, J. 1988, Nature, 332, 691
Jura, M. 2003, ApJ, 584, L91
Jura, M. 2006, ApJ, 653, 613
Jura, M., Farihi, J., Zuckerman, B., & Becklin, E. E. 2007, ApJ, 133, 1927
Kalas, P., Graham, J. R., & Clampin, M. 2005, Nature, 435, 1067
Kalas, P., Graham, J. R., Clampin, M. C., & Fitzgerald, M. P. 2006, ApJ, 637, L57
Keller, L., et al. 2002, Nature, 417, 148
Kemper, F., Jäger, C., Waters, L. B. F. M., Henning, Th., Molster, F. J., Barlow, M. J., Lim, T., & de Koter, A. 2002, Nature, 415, 295
Kilic, M., von Hippel, T., Leggett, S. K., & Winget, D. E. 2006, ApJ, 646, 474
Kimura, Y., Kurumada, M., Tamura, K., Koike, C., Chihara, H., & Kaito, C. 2005, A&A, 442, 507
Kleinman, S. J., et al. 1998, ApJ, 495, 424
Koester, D., Rollenhagen, K., Napiwotzki, R., Voss, B., Christlieb, N., Homeier, D., & Reimers, D. 2005, A&A, 432, 1025
Koike, C., Chihara, H., Tsuchiyama, A., Suto, H., Sogawa, H., & Okuda, H. 2003, A&A, 399, 1101
Li, A., & Draine, B. T. 2001, ApJ, 554, 778

Lisse, C. M., Beichman, C. A., Bryden, G., & Wyatt, M. C. 2007a, ApJ, 658, 584
Lisse, C. M., Chen, C. H., Wyatt, M. C., & Morlok, A. 2008, ApJ, 673, 1106
Lisse, C. M., Kraemer, K. E., Nuth, J. A., III, Li, A., & Joswiak, D. 2007b, Icarus, 187, 69
Lisse, C. M., et al. 2006, Science, 313, 635
Marcy, G., Butler, R. P., Fischer, D., Vogt, S., Wright, J. T., Tinney, C. G., & Jones, H. R. A. 2005, Prog. Theor. Phys. Suppl., 158, 24
Mathis, J. S. 1994, ApJ, 422, 176
Maxted, P. F. L., Napiwotzki, R., Dobbie, P. D., & Burleigh, M. R. 2006, Nature, 442, 543
Messenger, S., Sandford, S., & Brownlee, D. 2006, in Meteorites and the Early Solar System II, ed. D. S. Lauretta & H. Y. McSween, Jr. (Tucson, AZ: Univ. Arizona Press), 187–208
Molster, F. J., & Waters, L. B. F. M. 2003, in Lecture Notes in Physics (Berlin: Springer), 609, 121
Monnier, J. D., & Millan-Gabet, R. 2002, ApJ, 579, 694
O'Brien, D. P., & Greenberg, R. 2003, Icarus, 164, 334
Ogilvie, G. I., & Lin, D. N. C. 2007, ApJ, 661, 1180
Reach, W. T., Kuchner, M. J., von Hippel, T., Burrows, A., Mullally, F., Kilic, M., & Winget, D. E. 2005a, ApJ, 635, L161
Reach, W. T., et al. 2005b, PASP, 117, 978
Rhee, J. H., Song, I., Zuckerman, B., & McElwain, M. 2007, ApJ, 660, 1556
Sasselov, D. D. 2003, ApJ, 596, 1327
Scargle, J. D. 1982, ApJ, 263, 835
Schleicher, D. G., & A'Hearn, M. F. 1988, ApJ, 331, 1058
Shearer, C. K., Papike, J. J., & Rietmeijer, F. J. M. 1998, in Reviews in Mineralogy 36, Planetary Materials, ed. J. J. Papike (Washington: Mineralogical Society of America), 3
Su, K. Y. L., et al. 2007, ApJ, 657, L41
Trilling, D. E., et al. 2008, ApJ, 674, 1086
Vassiliadis, E., & Wood, P. R. 1993, ApJ, 413, 641
Vinković, D., Ivević, Z., Miroshnichenko, A. S., & Elitzer, M. 2003, MNRAS, 346, 1151
von Hippel, T., Kuchner, M. J., Kilic, M., Mullally, F., & Reach, W. T. 2007, ApJ, 662, 544
Werner, M. W., et al. 2004, ApJS, 154, 1
Weidemann, V. 2000, A&A, 363, 647
Weisberg, M. K., McCoy, T. J., & Krot, A. N. 2006, in Meteorites and the Early Solar System II, ed. D. S. Lauretta & H. Y. McSween, Jr. (Tucson, AZ: Univ. Arizona Press), 19
Winget, D. E. 1990, ApJ, 357, 630
Woodward, C. E., Kelley, M. S., Bockelée-Morvan, D., & Gehrz, R. D. 2007, ApJ, 671, 1065
Zubko, V. G., Mennella, V., Colangeli, L., & Bussoletti, E. 1996, MNRAS, 282, 1321